






Deep submarine infiltration of altered geothermal groundwater on the south Chilean Margin

Vincent J. Clementi ^{1✉}, Yair Rosenthal ^{1,2}, Samantha C. Bova ^{1,29}, Elizabeth K. Thomas ³, James D. Wright², Richard A. Mortlock², Owen C. Cowling³, Linda V. Godfrey², Laurel B. Childress ⁴ & Expedition 379T Scientists*

Submarine groundwater discharge is increasingly recognized as an important component of the oceanic geochemical budget, but knowledge of the distribution of this phenomenon is limited. To date, reports of meteoric inputs to marine sediments are typically limited to shallow shelf and coastal environments, whereas contributions of freshwater along deeper sections of tectonically active margins have generally been attributed to silicate diagenesis, mineral dehydration, or methane hydrate dissociation. Here, using geochemical fingerprinting of pore water data from Site J1003 recovered from the Chilean Margin during D/V *JOIDES Resolution* Expedition 379 T, we show that substantial offshore freshening reflects deep and focused contributions of meteorically modified geothermal groundwater, which is likely sourced from a reservoir ~2.8 km deep in the Aysén region of Patagonia and infiltrated marine sediments during or shortly after the last glacial period. Emplacement of fossil groundwaters reflects an apparently ubiquitous phenomenon in margin sediments globally, but our results now identify an unappreciated locus of deep submarine groundwater discharge along active margins with potential implications for coastal biogeochemical processes and tectonic instability.

¹Department of Marine and Coastal Sciences, Rutgers University, New Brunswick, NJ, USA. ²Department of Earth and Planetary Sciences, Rutgers University, Piscataway, NJ, USA. ³Department of Geology, University at Buffalo, Buffalo, NY, USA. ⁴International Ocean Discovery Program, Texas A&M University, College Station, TX, USA. ²⁹Present address: Department of Geological Sciences, San Diego State University, San Diego, CA, USA. *A list of authors and their affiliations appears at the end of the paper. ✉email: clementi@marine.rutgers.edu

A full account of the sources and sinks of solutes in the ocean is needed to constrain past and present biogeochemical cycles in the ocean. In recent decades, submarine groundwater discharge (SGD) has been shown to account for ≥ 5 –50 percent of riverine input for several important oceanic constituents^{1–3}. However, geochemical observations of SGD (e.g., ≥ 200 mM reductions in pore water Cl^- concentration) have largely been limited to shallow shelf settings on passive margins, with scarce evidence for SGD along deeper sections of continental slopes, on active margins, or in some of the most hydrologically dynamic regions on Earth^{4,5}. These data gaps intersect in Chile where despite model indications of high fluid discharge rates (≥ 1000 m^2 yr^{-1})^{6,7}, particularly in the southern sector of the country between 40–55°S, no observational evidence for SGD exists.

Chilean groundwaters range from glacially- or meteorically-recharged aquifers⁸ to deep geothermal reservoirs⁹. Steep catchment basins and rainfall exceeding 7500 mm yr^{-1} in southern Chile¹⁰ promote substantial recharge to kilometers depth through faulting in the bedrock¹¹. As a result, geothermal groundwaters in southern Chile can contain up to 50 percent meteoric fluid¹² and attain a chemical overprint, with dilute elemental concentrations (e.g., Cl^- near zero) and $^{18}\text{O}/^{16}\text{O}$ and $^2\text{H}/^1\text{H}$ isotope ratios ($\delta^{18}\text{O}$ and δD , respectively) that fall along the regional meteoric water line (MWL)^{13,14}. Widespread offshore freshening of pore waters on the Chilean Margin, as indicated by 20–200 mM reductions in Cl^- concentration compared to seawater, have been attributed to methane hydrate dissociation or mineral dehydration^{15,16}. However, these prior studies lack the isotopic constraints needed to diagnostically identify source fluids¹⁷, particularly to test for the infiltration of meteoric fluids in deep offshore sedimentary systems^{18–20}.

In this study, we investigate the cause of substantial pore water freshening at Site J1003 (45°28.5008'S, 75° 33.5020'W, 670 meters below sea level (mbsl)), which was drilled during D/V *JOIDES Resolution* Expedition 379T²¹. Site J1003 is located 50 kilometers offshore of the Taitao Peninsula at the southern terminus of the Chilean Coastal Range and upslope from the Chile Triple Junction (Fig. 1). The North Patagonia Ice Sheet is ~ 200 km SE of J1003, though it likely extended to the shelf break during the last glacial period²². The Andes and Coastal mountain ranges are separated by the Liquiñe-Ofqui fault zone (LOFZ), a 1000-kilometer intra-arc north-south oriented dextral strike-slip fault complex joined by four NE en échelon right-lateral fractures and with three NNW lineaments that extend seaward²³. High vertical permeability along the N-S and NE axes are conducive to vertical migration of deep geothermal groundwater¹¹. In contrast, NNW trending axes in Chile and elsewhere often have horizontal permeabilities that facilitate lateral fluid migration^{9,24}. Collectively, the LOFZ fault complex extends to ~ 10 km depth, promoting both vertical and horizontal fluid migration that manifests in the widespread distribution of thermal springs in the Aysén region of Patagonia¹¹. Fjord waters landward of J1003 have geochemical signatures indicative of partial mixing with meteoric and geothermal endmembers, reflecting the transport of meteorically altered geothermal groundwater through the LOFZ to surface locations¹³. Using elemental and isotopic fingerprinting in high-resolution sedimentary pore water samples from Site J1003²⁵, we reveal that the meteorically altered geothermal waters supplying thermal springs at surface locations in Patagonia have also infiltrated marine sediments on the Chilean Margin, accounting for a large degree of the observed pore water freshening.

Results and discussion

A geothermal groundwater source of freshened pore water. Pore water Cl^- concentrations at J1003 decrease from seawater

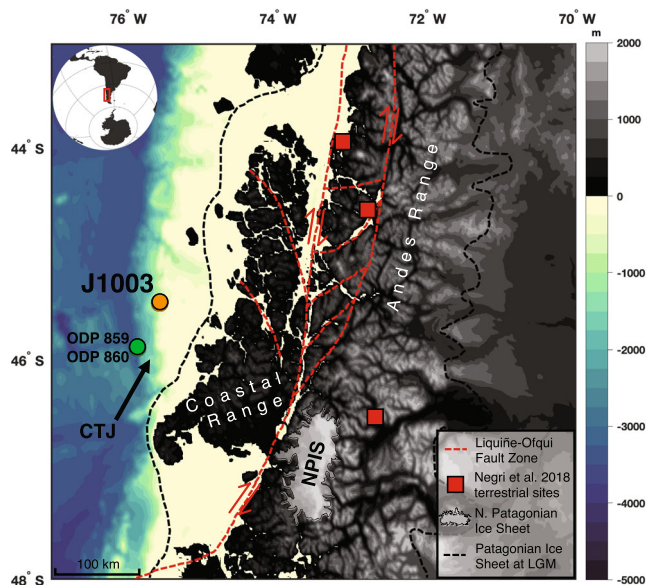


Fig. 1 Study setting. Map of the Chilean Margin showing the location of Expedition 379 T Site J1003 (orange). Shading shows regional bathymetric and topographic features at 250 m contour intervals. The modern extent of the North Patagonia Ice Sheet (NPIS; gray patch) and during the last glacial period (dotted black line) are shown²². Also shown are the two N-S, four NE, and NNW (two are present in this spatial range) lineaments that characterize the LOFZ (dotted red lines; modified after Cembrano et al. (ref. 23)) and the Chile Triple Junction (CTJ). Nearby ODP Sites 859 and 860 are marked in green. The Coastal and Andes mountain ranges are labeled. Red squares denote terrestrial hydrological study sites in Negri et al. (ref. 13).

values (~ 550 mM) at the sediment-seawater interface to ~ 360 mM at the base of the recovered sediment column (Fig. 2). The reduction in Cl^- concentration is paired with strong depletions in both $\delta^{18}\text{O}$ and δD , though the largest decreases occur below 20 meters below sea floor (mbsf). Likewise, Na^+ and K^+ concentrations mirror Cl^- , linearly decreasing by 28 and 25 percent from seawater values with depth, respectively. Ca^{2+} , Mg^{2+} , and Sr^{2+} concentrations also decrease with depth, but most of the reduction occurs within the upper 40 mbsf. $^{87}\text{Sr}/^{86}\text{Sr}$ becomes slightly less radiogenic (decreases) with depth, tracking many of the other profiles. In contrast, dissolved silica (DSi) concentrations increase downcore.

The depth profiles suggest that pore water at J1003 receives contributions from a freshened endmember depleted in most solutes and isotopes. Low pore water Cl^- concentrations observed in convergent margin settings have typically been attributed to methane hydrate dissociation and mineral dehydration, though anaerobic oxidation of methane, low temperature ocean-basalt interactions, clay membrane ion filtration, and SGD emplacement of fresh meteoric waters could also yield Cl^- concentrations substantially lower than seawater¹⁷. However, downcore decreases in Cl^- , $\delta^{18}\text{O}$, δD are not consistent with methane hydrate dissociation, mineral dehydration, anaerobic oxidation of methane, or fluid interactions with basalt as the primary controls on J1003 pore water chemistry, all of which tend to increase $\delta^{18}\text{O}$ and/or δD with depth^{17,26}.

Remaining processes that lower Cl^- , $\delta^{18}\text{O}$, and δD include clay membrane ion filtration and SGD. Clay filtration depletes expelled pore water in ions and heavy isotopes²⁷. Although Cl^- , Na^+ , K^+ , Ca^{2+} , Mg^{2+} , and Sr^{2+} concentrations all decrease with depth at J1003, DSi concentrations increase. Furthermore, ion filtration fractionates hydrogen more than oxygen, yielding a

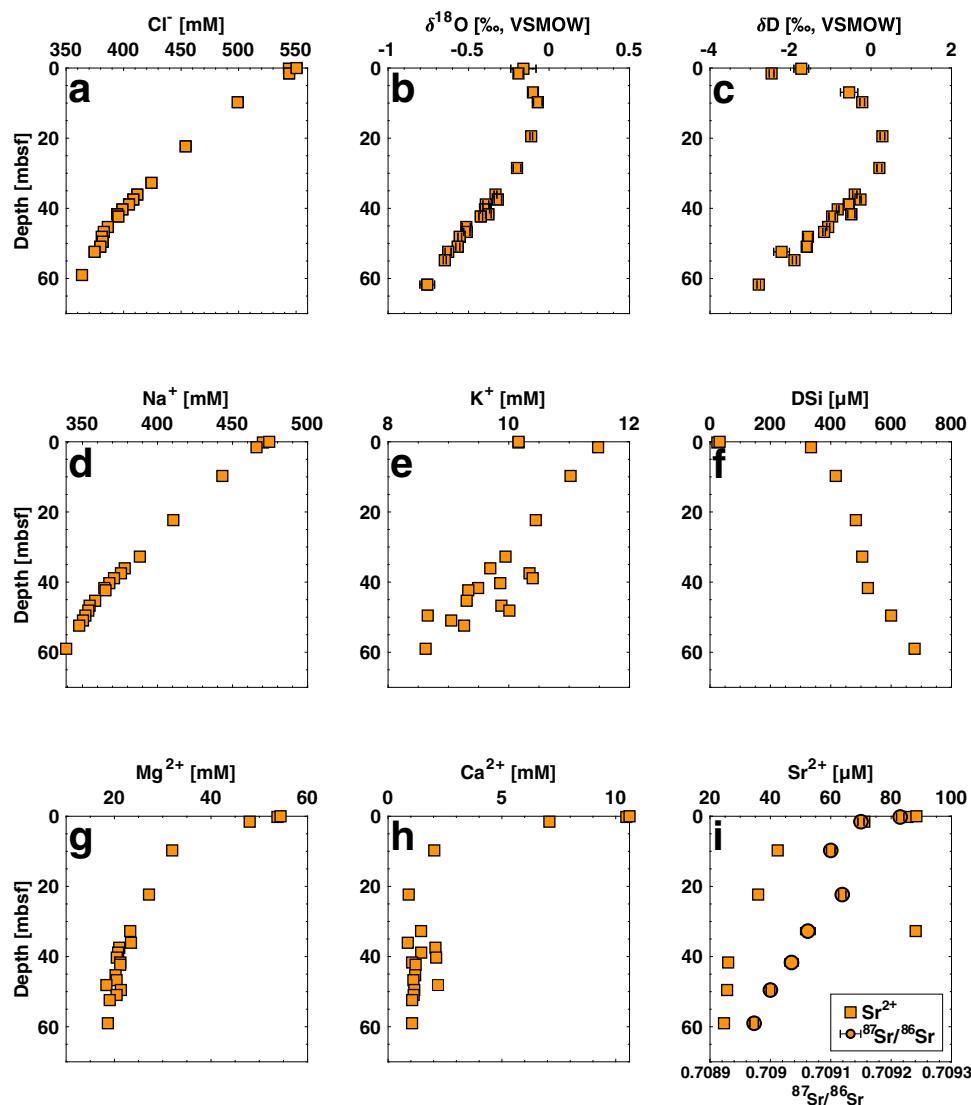


Fig. 2 Pore water geochemical profiles for J1003. **a** Chloride (Cl^-). **b** Oxygen isotope ratios ($\delta^{18}\text{O}$). **c** Deuterium isotope ratios (δD). **d** Sodium (Na^+). **e** Potassium (K^+). **f** Dissolved silica (DSi). **g** Magnesium (Mg^{2+}). **h** Calcium (Ca^{2+}). **i** Strontium (Sr^{2+}) in squares, strontium isotope ratios ($^{87}\text{Sr}/^{86}\text{Sr}$) in circles. Error bars in (a), (b), and (i) represent 1 standard deviation (1 SD) for each sample's analysis. Depth is plotted on the vertical axis in meters below sea floor (mbsf).

slope less than the MWL²⁸. In contrast, $\delta^{18}\text{O}$ and δD at J1003 fall on the MWL for Chile²⁹ (Fig. 3). Taken together, we rule out ion filtration, leaving deep SGD as the likely dominant source of low- Cl^- pore water at J1003.

To identify the groundwater source influencing J1003 sediments, we compared $\delta^{18}\text{O}$ and δD to Cl^- (Fig. 3). Previous studies highlight linear relationships between pore water O/H isotopes and Cl^- , which when extrapolated to the freshwater source ($\text{Cl}^- = 0$) can constrain the isotopic composition of the groundwater endmember^{18,19}. Instead, non-linearity between O/H isotopes and Cl^- is observed, suggesting secondary influences from an additional endmember that shifts downcore $\delta^{18}\text{O}$ and δD towards slightly enriched values while also contributing to marked freshening (Fig. 3).

Subsurface enrichment of $\delta^{18}\text{O}$ and δD has often been interpreted as the downward diffusion of the change in isotopic composition of seawater during the last glacial period, which also increased Cl^- by ~ 3 percent³⁰. However, the slight enrichment of $\delta^{18}\text{O}$ and δD at J1003 occurs without an increase in Cl^- concentration (Fig. 2). Instead, a likely candidate for the observed

non-linearity is methane hydrate dissociation, which increases $\delta^{18}\text{O}$ and δD and reduces Cl^- concentrations in pore water³¹. Lower-than-expected methane hydrate concentrations have been observed in accreted sediments downslope of J1003 owing to high heat flow from subduction at the Chile Triple Junction^{32,33}. Our results now provide geochemical evidence that active methane hydrate dissociation appears to be occurring off the Taitao Peninsula.

Projected endmember values for $\delta^{18}\text{O}$ ($-9.8 \pm 1.71\text{‰}$) and δD ($-70.6 \pm 17.5\text{‰}$) fall on the MWL and are in excellent agreement with modern precipitation data from southern Chile²⁹ and reported values from terrestrial sites in the Aysén region of Patagonia¹³ (Fig. 3d). The particularly strong agreement with geothermal groundwater and meteoric endmembers ($\delta^{18}\text{O}$: $-9.17 \pm 0.87\text{‰}$ and $-10.5 \pm 4.95\text{‰}$; δD : $-65.9 \pm 7.01\text{‰}$ and $-78.9 \pm 44.8\text{‰}$, respectively) is attributable to the meteoric overprint of geothermal groundwaters in the region and points to the deep submarine infiltration of these meteorically altered geothermal groundwaters on the Chilean Margin as the dominant source of freshening at J1003.

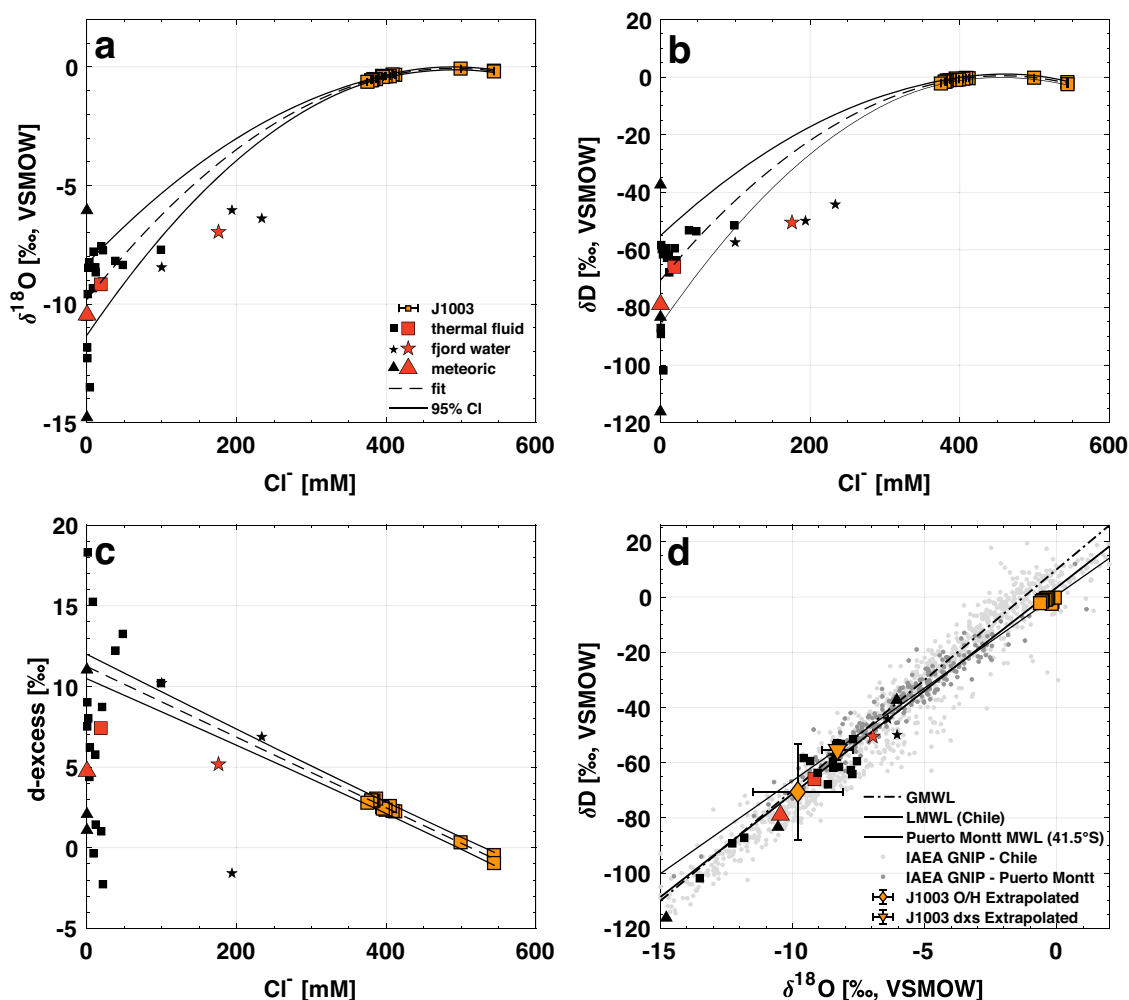


Fig. 3 Determining the groundwater origin. **a** $\delta^{18}\text{O}$ plotted against Cl^- . **b** δD plotted against Cl^- . **c** Deuterium excess (d-excess) plotted against Cl^- . For (a–c), the quadratic (a, b) and linear (c) fit is shown by the black dotted line, with 95% confidence intervals in black. **d** Comparison of $\delta^{18}\text{O}$ and δD with a compilation of meteoric values (gray) from Sanchez-Murillo et al. (ref. 29); data from Puerto Montt station are highlighted (dark gray). The global meteoric water line (GMWL, dotted) and those for Chile (solid), and Puerto Montt (thin) are shown. Measured data for J1003 are shown by the orange squares and extrapolated data by the orange diamond and inverted triangle (error bars represent 1SD). In all plots, data for thermal fluid (square), fjord water (star), and meteoric water (triangle) from the Aysén region reported by Negri et al. (ref. 13) are shown in black, averages for each subgroup are shown in red.

Support for the endmember estimates is provided by the linear extrapolation of deuterium excess (d-excess) to Cl^- equal to zero (Fig. 3c). The d-excess value of meteoric waters reflects the source conditions of water vapor³⁴, and in the Aysén region d-excess is largely controlled by the temperate climate conditions²⁹. However, estimates of endmember d-excess at J1003 ($+11.2 \pm 0.8$) are higher than observed values for modern meteoric waters in this region (e.g., $+7.7 \pm 5.8$ ‰ at Puerto Montt monitoring station), suggesting that the meteoric component of infiltrating groundwaters may have originated in a colder climate.

During the last glacial period, colder temperatures yielded more isotopically depleted precipitation and higher d-excess values³⁵. The d-excess endmember at J1003 could be produced by glacial-aged meteoric $\delta^{18}\text{O}$ and δD of -8.3 ± 0.5 ‰ and -55.3 ± 3.7 ‰, respectively, both of which are on the higher end but nonetheless consistent with endmember estimates at Cl^- equal to zero (Fig. 3a, b). Like the $\delta^{18}\text{O}$ - and δD -based endmember estimates, the d-excess endmember also falls on the regional MWL (Fig. 3d). The inferred 2.8‰ ^{18}O -depletion between the last glacial period and today is consistent with model-based estimates for this region³⁶, suggesting that freshened geothermal groundwaters may have been emplaced when the

Patagonian Ice Sheet (PIS) was more expansive than its modern configuration (Fig. 1)²². This adds to the growing body of evidence for fossil meteoric freshwater infiltrating marine sediments that sit proximal to ancient ice sheets in North America and Europe^{20,37}, but for the first time reveals that similar processes were associated with the PIS.

Finally, the (near-)linear relationships between Cl^- and Na^+ , K^+ , and DSi are best explained by binary mixing between seawater and the same geothermal groundwaters that supply thermal springs in the Aysén region of Patagonia¹³ (Fig. 4; Supplemental Fig. 1). These mixing models indicate a geothermal groundwater contribution of ~30 percent at the base of J1003. Pore water $^{87}\text{Sr}/^{86}\text{Sr}$ at J1003 is less radiogenic than seawater and can also be attributed to mixing with regional geothermal groundwaters, which are in isotopic equilibrium with the plutonic host rock¹². Using a geothermal groundwater endmember (0.7043) from the Villarrica region just north of J1003, which has a similar bedrock lithology as the Aysén region³⁸, a binary mixing model for $\delta^{18}\text{O}$ and $^{87}\text{Sr}/^{86}\text{Sr}$ yields a lower contribution of ~10 percent (Table 1; Supplementary Fig. 1). Nonetheless, meteorically altered geothermal groundwater contributions of 10–30 percent are sufficient to

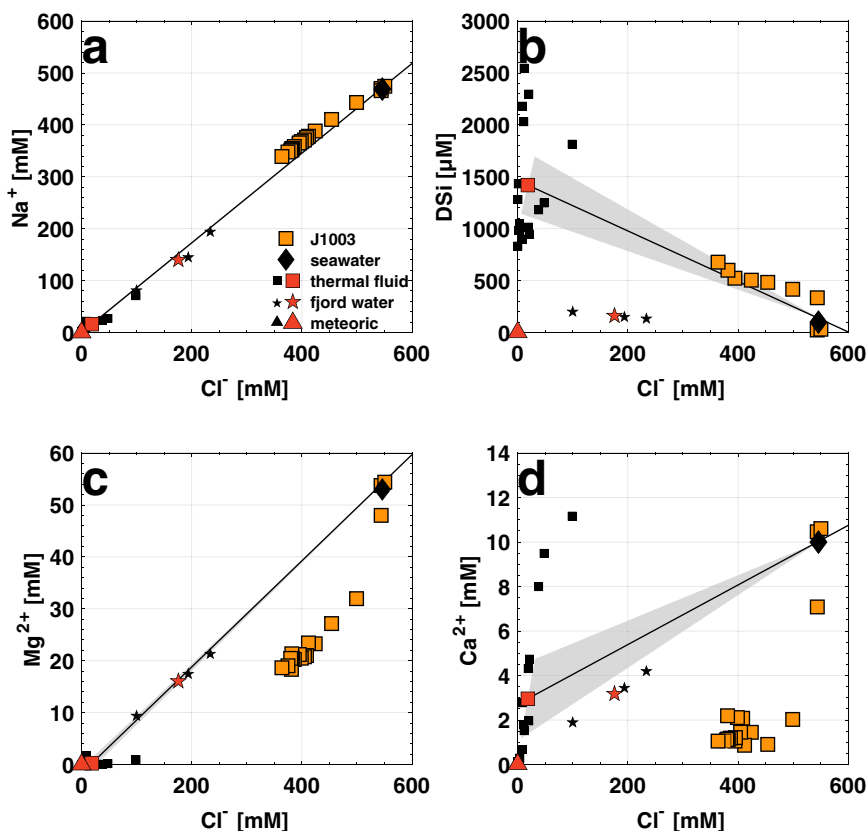


Fig. 4 Mixing between seawater and geothermal groundwater. **a** Cl^- against Na^+ . **b** Cl^- against DSi . **c** Cl^- against Mg^{2+} . **d** Cl^- against Ca^{2+} . Data for thermal fluid (square), fjord water (star), and meteoric water (triangle) from the Aysén region reported by Negri et al. (ref. ¹³) are shown in black; averages for each subgroup are shown in red. In all plots, mixing lines between geothermal groundwater and seawater (black diamonds) are shown, with gray windows highlighting the range of potential mixing lines derived from the minimum and maximum (95% confidence interval) endmember estimates.

Table 1 Mixing model parameters.

	Cl^-	Na^+	K^+	DSi	Ca^{2+}	Mg^{2+}	$\delta^{18}\text{O}$	δD	$^{87}\text{Sr}/^{86}\text{Sr}$
SW	544 mM	470 mM	10 mM	24 μM	10 mM	54 mM	-0.159‰	-1.7‰	0.7092
GT	18.5 ± 12.4 mM	16 ± 8.23 mM	0.523 ± 0.311 mM	1420 ± 276 μM	2.96 ± 1.78 mM	0.23 ± 0.229 mM	$-9.17 \pm 0.87\text{‰}$	$-65.9 \pm 7.01\text{‰}$	0.7043

Endmember values for seawater and geothermal groundwater used in the pore water mixing model, with the latter derived as the average of geothermal spring data from Negri et al. (ref. ¹³). For these, the error represents the 95% confidence interval based on the range of reported values, which are used to estimate the window of possible mixing lines shown in Fig. 4 and Supplementary Fig. 1. The geothermal groundwater $^{87}\text{Sr}/^{86}\text{Sr}$ and Sr^{2+} endmembers are from Held et al. (ref. ¹²). The midline elemental and isotopic composition is assumed to represent the seawater endmembers.

substantially modify the chemistry of sedimentary pore waters on the Chilean Margin.

Occurrence of dolomite. The binary mixing model fails to explain non-linear reductions in Ca^{2+} , Mg^{2+} , and Sr^{2+} concentrations (Fig. 4). Instead, these trends can be attributed to the precipitation of dolomite at depth, which was documented between 15–40 mbsf²¹. At high-sedimentation sites like J1003²¹, dolomitization occurs when sulfate is depleted and there is a sufficient Ca^{2+} and Mg^{2+} supply³⁹. Elevated methane concentrations in the upper sections of J1003 suggest that sulfate reduction is driven by biogenic degradation of organic matter, whereas decreasing C_1/C_2 ratios towards the base (attributable to high ethane concentrations) highlight a potential thermogenic influence at depth (Supplementary Fig. 2). Both mechanisms consume sulfate while also generating the requisite alkalinity. Furthermore, detrital silicates (high in adsorbed Mg^{2+}) readily undergo ion exchange with NH_4^+ generated during sulfate reduction^{40,41}, which potentially liberates the Mg^{2+} needed for dolomitization.

The dolomite-rich interval at J1003 coincides with sharp decreases in Ca^{2+} , Mg^{2+} , and Sr^{2+} concentrations and increased pore water $\text{Mg}^{2+}/\text{Ca}^{2+}$ and $\text{Sr}^{2+}/\text{Ca}^{2+}$ ratios (Fig. 2; Supplemental Fig. 3). Likewise, consumption of Sr^{2+} with little change in $^{87}\text{Sr}/^{86}\text{Sr}$ indicates a clear control from authigenic carbonate precipitation on Sr^{2+} concentrations (Supplementary Fig. 4), as documented on the Cascadia Margin⁴². Such changes are consistent with dolomitization and have been observed in dolomite-rich intervals on the nearby Peru Margin⁴³. In releasing H_2O , dolomitization may also contribute to observed freshening at J1003⁴⁴.

Decreases in pore water $^{87}\text{Sr}/^{86}\text{Sr}$ are attributable to binary mixing between geothermal groundwaters and seawater (Supplementary Fig. 1), but the slight decrease in $^{87}\text{Sr}/^{86}\text{Sr}$ could also (in part) reflect alteration of volcanogenic material, which was invoked to explain non-radiogenic $^{87}\text{Sr}/^{86}\text{Sr}$ at Ocean Drilling Program (ODP) Site 860, located 46 km downslope of J1003 (Fig. 1)⁴⁵. Volcanogenic material comprises 0–10 percent of the bulk sediment composition at J1003²¹. Although the formation of authigenic clays (e.g., smectite) from ash diagenesis could explain the observed decrease in Mg^{2+} concentrations, increases pore

water Cl^- , Ca^{2+} , and Sr^{2+} concentrations would be expected, none of which are reported at J1003 (Fig. 2). Further, smectite was determined to be a minor component of the bulk clay fraction at J1003²¹, consistent with previous characterizations of sediment composition in the region⁴⁶. It is plausible that Ca^{2+} and Sr^{2+} released by ash alteration are quickly consumed during dolomitization, and that any increase in Cl^- is overwhelmed by combined freshening effects from SGD, methane hydrate dissociation, and dolomite precipitation. However, comparison between pore water $^{87}\text{Sr}/^{86}\text{Sr}$ and the inverse Sr^{2+} concentration precludes ash alteration as an important control on pore water chemistry. Likewise, there is no evidence to support alteration of detrital material, which would yield more radiogenic $^{87}\text{Sr}/^{86}\text{Sr}$ (Supplementary Fig. 4). Instead, the robust binary mixing signal between $^{87}\text{Sr}/^{86}\text{Sr}$ and $\delta^{18}\text{O}$ and consumption of Sr^{2+} (and Ca^{2+} , Mg^{2+}) suggest that infiltration of altered geothermal groundwater, coupled with authigenic carbonate precipitation, are the more likely primary controls on strontium systematics at J1003, with ash diagenesis and formation of authigenic clays exerting only minor influences on pore water chemistry.

Constraints on the geothermal groundwater reservoir and fluid migration. The ratio of Na^+ and K^+ in thermal fluids reflects temperature-dependent ion exchange between geothermal groundwater and alkali feldspars (K^+ -feldspar, Na^+ -feldspar)⁴⁷, and this geothermometer has been employed to characterize geothermal groundwaters in southern Chile^{13,48}. If we assume that this method is also applicable in marine sediments that are influenced by geothermal groundwater, then pore water Na^+/K^+ can be used to estimate the reservoir temperature of geothermal groundwaters influencing J1003. Pore water-derived temperatures using four different equations are in excellent agreement with estimates from the Aysén thermal springs¹³ (e.g., J1003: 173.68 ± 2.06 °C; Aysén: 175 ± 14.3 °C; Supplementary Table 1), and further support a geothermal groundwater connection linking the Aysén region of Patagonia and the Chilean Margin.

With ~10–30 percent of pore water influenced by meteorically altered geothermal groundwater, we infer that freshwater delivery to J1003 must be sourced from a geothermal reservoir that is substantially deeper than the penetration depth of J1003. Indeed, the slightly concave down structure of the Cl^- profile suggests that fluid migration might be partly attributable to compaction-driven fluid advection from deeper in the sediment column (Fig. 2). Applying our Na^+/K^+ temperature estimates to the geothermal gradient at J1003 (53 °C km^{-1}), a reservoir depth of 2.82 ± 0.29 kmbsf is established (Supplementary Fig. 5). Although structural characterization of the geothermal reservoir in the Aysén region has not yet been conducted, this estimate agrees with those for the Tinguiririca geothermal reservoir in central Chile (2–6 kmbsf)^{48–50} and now provides a benchmark for future studies to test.

Despite considerable evidence for deep submarine discharge of meteorically altered geothermal groundwater at J1003, a fundamental question remains: How is this hydrogeologic connection established? Subsurface fluid migration in this region is primarily controlled by faulting within the LOFZ, with the NNW lineaments extending seaward serving as the most likely conduits for transporting groundwater offshore. Permeable early Quaternary coarse-grained strata at J1003²¹, Pliocene sandstone units to depths of 600 mbsf at nearby ODP Site 860⁵¹, and large permeability anisotropies at ODP Site 859⁵² indicate that structural features supporting horizontal fluid migration are also present in Chilean Margin sediments. Although the widespread distribution of thermal springs throughout the Aysén region suggests that the existing

hydraulic gradient is sufficient to support some amount of lateral geothermal groundwater migration through the LOFZ^{48,50} and potentially offshore today, higher-than-modern d-excess at J1003 suggest that groundwaters yielding low pore water Cl^- concentrations may have been emplaced during or shortly after the most recent glacial period.

During the last glaciation, the PIS was more expansive and ~100 times more voluminous than its current configuration²². Paired with a ~120 m lowering of global sea level, growth of the PIS would have substantially enhanced the hydraulic gradient between land and sea, facilitating the migration of groundwater offshore, as demonstrated in other margin settings proximal to ancient ice sheets^{4,5,19,20}. In the Aysén region, meteoric meltwater from the base of the PIS would have infiltrated the subsurface system through fractures and mixed with geothermal water at depth. This altered geothermal groundwater would have ultimately migrated through horizontally permeable pathways offshore, emplacing the distinct chemical signature in sediments near J1003.

Alternatively, emplacement of offshore groundwater could have occurred during the glacial termination. In this scenario, recharge of meteoric water from a retreating PIS through deeply extending faults and permeable strata might have allowed groundwater to penetrate the sedimentary system and migrate offshore. The timing of this would be consistent with the onset of hydrothermal activity in central Chile after the last glacial period⁵³, suggesting that reinvigoration of geothermal circulation may have occurred on a large scale in the region during the glacial termination. However, submarine discharge of altered geothermal groundwater during the deglacial period would have had to compete with a diminishing hydraulic gradient as sea levels rose and the PIS retreated from its maximum extent. Thus, we consider this the less likely of the two SGD scenarios.

Conclusions

Our chemical results from marine pore waters demonstrate that migration of geothermal groundwaters not only feeds thermal springs at the surface in the Aysén region of Patagonia but also simultaneously delivers freshened groundwater to offshore sediments. The absence of similar pore water features at nearby ODP Sites 859 (2760 mbsl) and 860 (2157 mbsl)⁴⁵ provide first-order depth and spatial constraints on this phenomenon and suggest that infiltration of groundwater to the Chilean Margin may be focused, potentially aided by faulting within the accretionary prism⁵⁴. This constitutes one of the deeper examples of SGD globally, but is not without precedent (e.g., ODP Leg 122 Site 760, 1970 mbsl, NW Australia⁵⁵) and adds to a growing body of geochemical evidence for the SGD along active and passive margins^{18–20,37}. Locally, our depth estimates for the Aysén geothermal reservoir may be of particular interest for efforts to harness geothermal energy for societal consumption. Globally, freshening in over pressurized accreted sediments on active margins can influence the mechanics of shallow-slip tectonism and potentially contribute to mega-thrust earthquakes that are commonly experienced in Chile and elsewhere⁵⁶. Indeed, similar links between meteoric freshening and tectonism may operate on the Cascadia, Nankai, and Okhotsk margins, where meteorically altered geothermal groundwaters^{57,58} and pore water trends similar to J1003^{59,60} have been reported.

Methods

Sample collection. Pore water samples were taken from whole round samples that were immediately collected from the bottom 5–10 cm of each core section upon recovery to the catwalk, yielding a sampling resolution of ~1.5 m. In addition, one mudline sample was collected from Holes A and B in J1003. Retrieved whole rounds were capped and transferred to the shipboard geochemistry laboratory for

immediate processing. In total, 40 samples were taken from J1003, with 18 samples analyzed onboard. The remainder of the pore water samples were split (~4–10 mL each), sealed in airtight glass vials, and archived for shore-based analysis.

For samples that underwent shipboard analysis, the following measures were taken. First, the sediment surface of each whole round was carefully scraped to mitigate possible contamination. Next, the whole round sample was placed in a titanium hydraulic press and subjected to 35,000 lb force for interstitial water extraction. Upon extraction, pore water was filtered through a Whatman No. 1 filter (11 µm) and 0.5 mL was discarded to avoid contamination. The remainder of fluid was filtered into a sterile syringe and filtered again through a 0.45 µm polysulfone filter.

Shipboard pore water elemental and ion analysis. Shipboard analysis of J1003 pore waters followed protocols outlined in Gieskes et al. (ref. 61), Murray et al. (ref. 62), and the International Ocean Discovery Program user manual for shipboard instrumentation. Major cations (Na⁺, Ca²⁺, Mg²⁺, K⁺) and anions (Cl⁻, SO₄²⁻) were measured on pore water samples (n = 18) using a shipboard Metrohm 850 ion chromatographer (IC). Dissolved ammonium (NH₄⁺) concentrations were determined using an Agilent Cary Series 100 UV-visible spectrophotometer fitted with an Agilent SPS3 autosampler. Alkalinity was determined immediately after squeezing by Gran titration with an autotitrator (Metrohm 794 basic Titrino) using 0.1 M HCl at 25 °C. Certain trace elements (Sr²⁺, DSI) were measured using a shipboard Agilent 5110 SVDV ICP-AES (n = 8). Precision (1σ) based on repeated measurements on IAPSO and internal standards were <3.5% for IC measurements, <3.4% for NH₄⁺, and <2% for alkalinity. Reproducibility for ICP-AES measurements was ~1% for all reported elements. We refer the reader to the Expedition 379 T Preliminary Report²¹ for additional details on shipboard inorganic geochemical analysis of interstitial water samples.

Shipboard hydrocarbon gas analysis. Sediment gas composition was determined at a resolution of 1 sample per core for J1003 (n = 9). A 3 cm³ bulk sediment sample was collected from freshly exposed top end of a core section using a brass boring tool immediately after core recovery on the catwalk. The sediment plug was placed in a glass vial and sealed with an aluminum cap fitted with a PTFE/silicon septa for transfer to the shipboard geochemistry laboratory. The vial was heated to 70 °C for 30 min to evolve hydrocarbon gases from the sediment. A 5 cm³ volume of headspace gas was extracted from the sealed vial using a gas-tight 5 mL PTFE Luer lock glass syringe and injected into an Agilent/HP 6890 Series II Gas Chromatograph fitted with a flame ionization detector for analysis. Concentrations of methane (CH₄) and higher molecular weight hydrocarbons were determined and reported as parts per million by volume (ppmv) of the injected sample.

Shore-based pore water δ¹⁸O, δD, and ⁸⁷Sr/⁸⁶Sr analyses. Pore water δ¹⁸O and δD were determined (n = 23) using a Picarro L2130-i cavity ringdown laser spectrometer light isotope instrument in triplicates at the University at Buffalo following methods in van Geldern and Barth⁶³. Samples were injected four times and each injection was corrected for memory and drift, and were then normalized to Vienna Standard Mean Ocean Water (VSMOW). The first injection was discarded for each sample and the remaining three analyses were aggregated into an average value with associated replicate uncertainty. Average replicate standard deviation (1 SD) was 0.02‰ for δ¹⁸O measurements and 0.08‰ for δD measurements.

Additional pore water δ¹⁸O measurements (n = 26) were made at the Rutgers University Stable Isotope Laboratory using a FISIONS OPTIMA Mass Spectrometer equipped with a MicroMass Multiprep automatic sample processing system after water equilibration with CO₂ using standard methods^{64,65}. All samples were run in duplicate. Reproducibility is estimated to be ±0.04‰ (1 SD) as determined by multiple (n = 12) daily analyses of laboratory standards. Accuracy is estimated to be within 0.03‰ by comparison of North Atlantic Bottom Water with VSMOW. δ¹⁸O determined on the Picarro show excellent agreement with a higher resolution record determined with IR-MS (Supplementary Fig. 6).

Pore water ⁸⁷Sr/⁸⁶Sr analysis (n = 8) followed the Sr separation protocol of Horwitz et al.⁶⁶. Sample volumes were calculated from shipboard elemental concentrations, targeting at least 1 µg Sr for each sample. Sample fluid was acidified to 2 N using 7 N HNO₃ prior to separation. Strontium was chromatographically separated from the pore water matrix using Eichrom 50–100 µm Sr Resin and different concentrations of HNO₃. Strontium was collected in 0.5 N HNO₃ in acid cleaned 3 mL Saville vials, dried down, and then dissolved in 2% by volume HNO₃ for analysis. Samples were analyzed in a wet plasma using a ThermoScientific Neptune Plus MC-ICP-MS at Rutgers University. Sr isotopes were corrected for fractionation using the measured ⁸⁸Sr/⁸⁶Sr ratio of 8.3752. NIST SRM 987, which was analyzed multiple times during sample analyses, yielded an ⁸⁷Sr/⁸⁶Sr ratio of 0.710274 ± 0.000007 (2 SD, n = 33).

Binary mixing model. By assuming that pore waters at J1003 are not altered by diagenetic reactions or other mixing processes, the elemental and isotopic composition of two pore fluid constituents in a two-endmember mixed fluid was

linearly correlated following Kastner et al.⁴³. Briefly,

$$Y_{IW} = X_{IW} \frac{Y_{GT} - Y_{SW}}{X_{GT} - X_{SW}} + \frac{Y_{SW}X_{GT} - Y_{GT}X_{SW}}{X_{GT} - X_{SW}}$$

where X and Y correspond to the elemental concentration or isotopic ratio of pore water constituents being considered (e.g., Cl⁻ and Na⁺, δ¹⁸O and ⁸⁷Sr/⁸⁶Sr). Subscripts refer to interstitial water (IW), geothermal groundwater (GT), and seawater (SW). In Fig. 4, X refers to Cl⁻ concentrations and X_{IW} is treated as a single step range of Cl⁻ from 18.5–540 mM.

Data availability

The source data for J1003 shown in Fig. 2 can be found online at the Zenodo repository (<https://doi.org/10.5281/zenodo.6525350>). All correspondence and data requests should be addressed to V.J.C.

Received: 19 January 2022; Accepted: 26 August 2022;

Published online: 21 September 2022

References

- Moore, W. S. The effect of submarine groundwater discharge on the ocean. *Ann. Rev. Marine Sci.* **2**, 59–88 (2010).
- Mayfield, K. K. et al. Groundwater discharge impacts marine isotope budgets of Li, Mg, Ca, Sr, and Ba. *Nat. Commun.* **12**, 9 (2021).
- Rahman, S., Tamborski, J. J., Charette, M. A. & Cochran, J. K. Dissolved silica in the subterranean estuary and the impact of submarine groundwater discharge on the global marine silica budget. *Marine Chem.* **208**, 29–42 (2019).
- Micallef, A. et al. Offshore freshened groundwater in continental margins. *Rev. Geophys.* **59** <https://doi.org/10.1029/2020rg000706> (2021).
- Post, V. E. A. et al. Offshore fresh groundwater reserves as a global phenomenon. *Nature* **504**, 71–78 (2013).
- Luijendijk, E., Gleeson, T. & Moosdorf, N. Fresh groundwater discharge insignificant for the world's oceans but important for coastal ecosystems. *Nature Communications* **11**, 12 (2020).
- Zhou, Y. Q., Sawyer, A. H., David, C. H. & Famiglietti, J. S. Fresh Submarine Groundwater Discharge to the Near-Global Coast. *Geophys. Res. Lett.* **46**, 5855–5863 (2019).
- Taucare, M., Daniele, L., Viguier, B., Vallejos, A. & Arancibia, G. Groundwater resources and recharge processes in the Western Andean Front of Central Chile. *Sci. Total Environ.* **722**, 137824 (2020).
- Daniele, L. et al. Exploring the shallow geothermal resources in the Chilean Southern Volcanic Zone: Insight from the Lique thermal springs. *J. Geochem. Exploration* **218** <https://doi.org/10.1016/j.gexplo.2020.106611> (2020).
- Garreaud, R., Lopez, P., Minvielle, M. & Rojas, M. Large-scale control on the Patagonian climate. *J. Clim.* **26**, 215–230 (2013).
- Sanchez, P., Perez-Flores, P., Arancibia, G., Cembrano, J. & Reich, M. Crustal deformation effects on the chemical evolution of geothermal systems: the intra-arc Lique-Ofqui fault system, Southern Andes. *Int. Geology Rev.* **55**, 1384–1400 (2013).
- Held, S. et al. Geochemical characterization of the geothermal system at Villarrica volcano, Southern Chile; Part 1: Impacts of lithology on the geothermal reservoir. *Geothermics* **74**, 226–239 (2018).
- Negri, A. et al. Decoding fjord water contribution and geochemical processes in the Aysen thermal springs (Southern Patagonia, Chile). *J. Geochem. Exploration* **185**, 1–13 (2018).
- Wrage, J. et al. Geochemistry of thermal waters in the Southern Volcanic Zone, Chile - Implications for structural controls on geothermal fluid composition. *Chem. Geology* **466**, 545–561 (2017).
- Mix, A. C., Tiedemann, R., Blum, P. & Participants, A. C. Initial Reports. *Proceedings of the Ocean Drilling Program* **202** <https://doi.org/10.2973/odp.proc.ir.202.2003> (2003).
- Scholz, F., Hensen, C., Schmidt, M. & Geersen, J. Submarine weathering of silicate minerals and the extent of pore water freshening at active continental margins. *Geochimica et Cosmochimica Acta* **100**, 200–216 (2013).
- Kastner, M., Elderfield, H. & Martin, J. B. Fluids in convergent margins - what do we know about their composition, origin, role in diagenesis and importance for oceanic chemical fluxes. *Philos. Trans. R. Soc. Lond. Ser. a-Math. Phys. Eng. Sci.* **335**, 243–259 (1991).
- Gwiazda, R. et al. Freshwater seepage into sediments of the shelf, shelf edge, and continental slope of the Canadian Beaufort Sea. *Geochemistry Geophysics Geosystems* **19**, 3039–3055 (2018).

19. Kriete, C., Suckow, A. & Harazim, B. Pleistocene meteoric pore water in dated marine sediment cores off Callao, Peru. *Estuarine Coastal and Shelf Science* **59**, 499–510 (2004).
20. Hong, W. L. et al. Discharge of meteoric water in the Eastern Norwegian Sea since the Last Glacial Period. *Geophys. Res. Lett.* **46**, 8194–8204 (2019).
21. Bova, S. C. et al. Expedition 379T Preliminary Report, Digging Deeper with the JR100: Extending high resolution paleoclimate records from the Chilean Margin to the Eemian. *Zenodo* <https://doi.org/10.5281/zenodo.5553428> (2019).
22. Hulton, N. R. J., Purves, R. S., McCulloch, R. D., Sugden, D. E. & Bentley, M. J. The Last Glacial Maximum and deglaciation in southern South America. *Quaternary Sci. Rev.* **21**, 233–241 (2002).
23. Cembrano, J., Herve, F. & Lavenu, A. The Liquine Ofqui fault zone: A long-lived intra-arc fault system in southern Chile. *Tectonophysics* **259**, 55–66 (1996).
24. Barton, C. A., Zoback, M. D. & Moos, D. Fluid-flow along potentially active faults in crystalline rock. *Geology* **23**, 683–686 (1995).
25. Clementi, V. J. et al. Pore water and headspace gas data for Site J1003 (Chilean Margin). *Zenodo* <https://doi.org/10.5281/zenodo.6525350> (2022).
26. Dahlmann, A. & de Lange, G. J. Fluid-sediment interactions at Eastern Mediterranean mud volcanoes: a stable isotope study from ODP Leg 160. *Earth Planet. Sci. Lett.* **212**, 377–391 (2003).
27. Hanshaw, B. B. & Coplen, T. B. Ultrafiltration by a compacted clay membrane—Part 2: Sodium ion exclusion at various ionic strengths. *Geochimica Et Cosmochimica Acta* **37**, 2311–2327 (1973).
28. Coplen, T. B. & Hanshaw, B. B. Ultrafiltration by a compacted clay membrane—Part 1: Oxygen and hydrogen isotopic fractionation. *Geochimica Et Cosmochimica Acta* **37**, 2295–2310 (1973).
29. Sanchez-Murillo, R. et al. in *Andean Hydrology* (eds D. A. Rivera, A. GodoyFaundez, & M. LilloSaavedra) 205–230 (Crc Press-Taylor & Francis Group, 2018).
30. Adkins, J. F., McIntyre, K. & Schrag, D. P. The salinity, temperature, and $\delta^{18}\text{O}$ of the glacial deep ocean. *Science* **298**, 1769–1773 (2002).
31. Ussler, W. & Paull, C. K. Effects of ion-exclusion and isotopic fractionation on pore-water geochemistry during gas hydrate formation and decomposition. *Geo-Marine Lett.* **15**, 37–44 (1995).
32. Villar-Muñoz, L. et al. Gas hydrate estimate in an area of deformation and high heat flow at the Chile triple junction. *Geosciences*, **9** <https://doi.org/10.3390/geosciences9010028> (2019).
33. Brown, K. M. et al. in *Proceedings of the Ocean Drilling Program, Scientific Results* Vol. 141 (eds S.D. Lewis, J. H. Behrmann, R. J. Musgrave, & S.C. Cande) 363–372 (1995).
34. Dansgaard, W. Stable isotopes in precipitation. *Tellus* **16**, 436–468 (1964).
35. Jasechko, S. et al. Late-glacial to late-Holocene shifts in global precipitation $\delta^{18}\text{O}$. *Clim. Past* **11**, 1375–1393 (2015).
36. Jasechko, S. Late-Pleistocene precipitation $\delta^{18}\text{O}$ interpolated across the global landmass. *Geochem. Geophys. Geosyst.* **17**, 3274–3288 (2016).
37. van Geldern, R. et al. Stable isotope geochemistry of pore waters and marine sediments from the New Jersey shelf: Methane formation and fluid origin. *Geosphere* **9**, 96–112 (2013).
38. Pankhurst, R. J., Weaver, S. D., Herve, F. & Larrondo, P. Mesozoic–Cenozoic evolution of the North Patagonian Batholith in Aysen, southern Chile. *J. Geological Soc.* **156**, 673–694 (1999).
39. Baker, P. A. & Kastner, M. Constraints on the formation of sedimentary dolomite. *Science* **213**, 214–216 (1981).
40. Moore, G. W. & Gieskes, J. M. Interaction between sediment and interstitial water near the Japan Trench, Leg 57, Deep Sea Drilling Project. *Init. Reps. DSDP* **56–57**, 1269–1276 (1980).
41. Vonbreyman, M. T. & Suess, E. Magnesium in the marine sedimentary environment: Mg-NH₄ ion exchange. *Chem. Geology* **70**, 359–371 (1988).
42. Teichert, B. M. A., Torres, M. E., Bohrmann, G. & Eisenhauer, A. Fluid sources, fluid pathways and diagenetic reactions across an accretionary prism revealed by Sr and B geochemistry. *Earth Planet. Sci. Lett.* **239**, 106–121 (2005).
43. Kastner, M. et al. Diagenesis and interstitial water chemistry at the Peruvian continental margin: Major constituents and strontium isotopes. *Proc. Ocean Drilling Progr.* **112**, 413–440 (1990).
44. Morrow, D. W. Dolomite—Part 1: The chemistry of dolomitization and dolomite precipitation. *Geoscience Canada* **9**, 5–13 (1982).
45. Zheng, Y., Froelich, P. N., Torres, M. E. & Dia, A. N. in *Proceedings of the Ocean Drilling Program, Scientific Results* Vol. 141 (eds S.D. Lewis, J. H. Behrmann, R. J. Musgrave, & S.C. Cande) (1995).
46. Lamy, F., Hebbeln, D. & Wefer, G. Terrigenous sediment supply along the Chilean continental margin: modern regional patterns of texture and composition. *Geol Rundsch* **87**, 477–494 (1998).
47. Giggenbach, W. F. Geothermal solute equilibria. Derivation of Na-K-Mg-Ca geothermometers. *Geochimica et Cosmochimica Acta* **52**, 2749–2765 (1988).
48. Benavente, O. et al. Chemical and isotopic features of cold and thermal fluids discharged in the Southern Volcanic Zone between 32.5 degrees S and 36 degrees S: Insights into the physical and chemical processes controlling fluid geochemistry in geothermal systems of Central Chile. *Chem. Geology* **420**, 97–113 (2016).
49. Pavez, C. et al. Characterization of the hydrothermal system of the Tinguiririca Volcanic Complex, Central Chile, using structural geology and passive seismic tomography. *J. Volcanol. Geother. Res.* **310**, 107–117 (2016).
50. Pearce, R. K. et al. Reactivation of fault systems by compartmentalized hydrothermal fluids in the southern andes revealed by magnetotelluric and seismic data. *Tectonics* **39**, e2019TC005997 (2020).
51. Behrmann, J., Lewis, S. D., Musgrave, R. J. & Party, S. S. Proc. Ocean Drill. Prog. Initial Rep. 141. Ocean Drilling Program, College Station TX (1992).
52. Brown, K. M. & Bangs, N. L. Thermal regime of the Chile Triple Junction: Constraints provided by downhole temperature measurements and distribution of gas hydrate. *Proc. Ocean Drilling Program Sci. Results* **141**, 259–275 (1995).
53. Munoz-Saez, C. et al. Radiocarbon Dating of Silica Sinter and Postglacial Hydrothermal Activity in the El Tatio Geyser Field. *Geophys. Res. Lett.* **47** <https://doi.org/10.1029/2020gl087908> (2020).
54. Moore, J. C. & Vrolijk, P. Fluids in accretionary prisms. *Rev. Geophys.* **30**, 113–135 (1992).
55. De Carlo, E. H. in *Proceedings of the Ocean Drilling Program* Vol. 122 (eds U. von Rad, B.U. Haq, & S. O'Connell) 295–308 (1992).
56. Aretusini, S., Meneghini, F., Spagnuolo, E., Harbord, C. W. & Di Toro, G. Fluid pressurisation and earthquake propagation in the Hikurangi subduction zone. *Nat. Commun.* **12** <https://doi.org/10.1038/s41467-021-22805-w> (2021).
57. Golla, J. K. & Tepper, J. H. Comparison and controls of thermal spring chemistry in Cascade Range and Olympic Mountains geothermal provinces, Washington. *Geother. Resour. Council Trans.* **41**, 1438–1454 (2017).
58. Bragin, I. V., Zippa, E. V., Chelnokov, G. A. & Kharitonova, N. A. Estimation of the Deep Geothermal Reservoir Temperature of the Thermal Waters of the Active Continental Margin (Okhotsk Sea Coast, Far East of Asia). *Water* **13** <https://doi.org/10.3390/w13091140> (2021).
59. Tomaru, H., Torres, M. E., Matsumoto, R. & Borowski, W. S. Effect of massive gas hydrate formation on the water isotopic fractionation of the gas hydrate system at Hydrate Ridge, Cascadia margin, offshore Oregon. *Geochem. Geophys. Geosyst.* **7**, n/a–n/a (2006).
60. Toki, T., Tsunogai, U., Gamo, T., Kuramoto, S. & Ashi, J. Detection of low-chloride fluids beneath a cold seep field on the Nankai accretionary wedge off Kumano, south of Japan. *Earth Planetary Sci Lett.* **228**, 37–47 (2004).
61. Gieskes, J., Gamo, T. & Brumsack, H. J. Chemical methods for interstitial water analysis aboard JOIDES Resolution. *ODP Technical Note* **15** (1991).
62. Murray, R. W., Miller, D. J. & Kryc, K. A. Analysis of major and trace elements in rocks, sediments, and interstitial waters by inductively coupled plasma-atomic emission spectrometry (ICP-AES). *ODP Technical Note* **29** (2000).
63. van Geldern, R. & Barth, J. A. C. Optimization of instrument setup and post-run corrections for oxygen and hydrogen stable isotope measurements of water by isotope ratio infrared spectroscopy (IRIS). *Limnol. Oceanogr.-Methods* **10**, 1024–1036 (2012).
64. Epstein, S. & Mayeda, T. Variation of O18 content of waters from natural sources. *Geochimica et Cosmochimica Acta* **4**, 213–224 (1953).
65. Fairbanks, R. G. The origin of continental shelf and slope water in the New York Bight and Gulf of Mexico: evidence from H₂¹⁸O/H₂¹⁶O ratio measurements. *J. Geophys. Res.* **87**, 5796–5808 (1982).
66. Horwitz, E. P., Chiarizia, R. & Dietz, M. L. A novel strontium-selective extraction chromatographic resin. *Solvent Extract. Ion Exchange* **10**, 313–336 (1992).

Acknowledgements

We would like to thank the captain and crew of the D/V *JOIDES Resolution* and JRSO for their tireless efforts during the inaugural JR100 expedition. The expedition and study were funded by NSF grant OCE-1756241 to S.C.B. and Y.R., a grant from the International Association of GeoChemistry to V.J.C., and a Methane Hydrates Graduate Fellowship from the National Research Council-National Energy Technology Laboratory to V.J.C. O.C.C. was supported by NSF grant EAR-IF-1652274 to E.K.T. We thank R. Sherrell, L. Herbert, and S. Ko for fruitful discussions and three reviewers for their constructive feedback, which have greatly strengthened this manuscript.

Author contributions

V.J.C. and Y.R. designed the experiment. V.J.C. carried out shore-based geochemical analyses (with contributions from E.K.T., J.D.W., R.A.M., O.C.C., and L.V.G.), prepared figures, and wrote the initial manuscript. S.C.B., Y.R., and L.B.C. organized and managed the expedition. The Expedition 379 T science party contributed to the collection and

generation of shipboard data. All named authors contributed to the interpretation of data and revisions of this manuscript.

Publisher's note Springer Nature remains neutral with regard to jurisdictional claims in published maps and institutional affiliations.

Competing interests

The authors declare no competing interests.

Additional information

Supplementary information The online version contains supplementary material available at <https://doi.org/10.1038/s43247-022-00541-3>.

Correspondence and requests for materials should be addressed to Vincent J. Clementi.

Peer review information *Communications Earth & Environment* thanks Wei-Li Hong and the other, anonymous, reviewer(s) for their contribution to the peer review of this work. Primary Handling Editors: Olivier Sulpis, Joe Aslin. Peer reviewer reports are available.

Reprints and permission information is available at <http://www.nature.com/reprints>



Open Access This article is licensed under a Creative Commons Attribution 4.0 International License, which permits use, sharing, adaptation, distribution and reproduction in any medium or format, as long as you give appropriate credit to the original author(s) and the source, provide a link to the Creative Commons license, and indicate if changes were made. The images or other third party material in this article are included in the article's Creative Commons license, unless indicated otherwise in a credit line to the material. If material is not included in the article's Creative Commons license and your intended use is not permitted by statutory regulation or exceeds the permitted use, you will need to obtain permission directly from the copyright holder. To view a copy of this license, visit <http://creativecommons.org/licenses/by/4.0/>.

© The Author(s) 2022

Expedition 379T Scientists

Ivano W. Aiello⁵, Alejandro Avila⁶, William Biggs¹, Christopher D. Charles⁷, Anson H. Cheung⁸, Kimberly deLong⁹, Isabel A. Dove¹⁰, Xiaojing Du^{8,11}, Emily R. Estes⁴, Ursula Fuentes¹², Cristina García-Lasanta¹³, Steven L. Goldstein¹⁴, Anna Golub^{7,15}, Julia Rieke Hagemann¹⁶, Robert G. Hatfield¹⁷, Laura L. Haynes¹⁸, Anya V. Hess², Nil Irvali¹⁹, Yael Kiro²⁰, Minda M. Monteagudo²¹, Jonathan E. Lambert¹⁴, Chen Li²², William M. Longo^{23,24}, Sarah McGrath⁸, Hailey Riechelson¹, Rebecca S. Robinson¹⁰, John Sarao²⁵, Adam D. Sproson²⁶, Shawn Taylor²⁷, Yusuke Yokoyama²⁸ & Siyao M. Yu²

⁵Moss Landing Marine Laboratories, Moss Landing, CA, USA. ⁶Center for Oceanographic Research in the Eastern South Pacific (FONDAP-COPAS), University of Concepción, Concepción, Chile. ⁷Scripps Institution of Oceanography, University of California, San Diego, La Jolla, CA, USA.

⁸Department of Earth, Environmental, and Planetary Sciences, Brown University, Providence, RI, USA. ⁹Ocean Sciences Department, University of California, Santa Cruz, Santa Cruz, CA, USA. ¹⁰University of Rhode Island Graduate School of Oceanography, Narragansett, RI, USA. ¹¹Institute at Brown for Environment and Society, Providence, RI, USA. ¹²Hydrographic and Oceanographic Services, Chilean Navy, Valparaíso, Chile. ¹³Geology Department, Western Washington University, Bellingham, WA, USA. ¹⁴Lamont-Doherty Earth Observatory, Columbia University, Palisades, NY, USA. ¹⁵Department of Geology and Environmental Geoscience, Lafayette College, Easton, PA, USA. ¹⁶Department of Marine Geology and Paleontology, Alfred Wegener Institute Helmholtz Center for Polar and Marine Research, Bremerhaven, Germany. ¹⁷Department of Geological Sciences, University of Florida, Gainesville, FL, USA. ¹⁸Department of Earth Science and Geography, Vassar College, Poughkeepsie, NY, USA. ¹⁹Department of Earth Science and Bjerknes Centre for Climate Research, University of Bergen, Bergen, Norway. ²⁰Department of Earth and Planetary Sciences, Weizmann Institute of Science, Rehovot, Israel. ²¹School of Earth and Atmospheric Sciences, Georgia Institute of Technology, Atlanta, GA, USA. ²²State Key Laboratory of Marine Geology, Tongji University, Shanghai, China. ²³Department of Environmental Studies, Macalester College, Saint Paul, MN, USA. ²⁴Division of Environmental Health Sciences, University of Minnesota, Minneapolis, MN, USA. ²⁵College of Geosciences, Texas A&M University, College Station, TX, USA. ²⁶Biogeochemistry Research Center, JAMSTEC, Yokosuka, Japan. ²⁷Department of Geological Sciences and Environmental Studies, Binghamton University, Binghamton, NY, USA. ²⁸Atmosphere and Ocean Research Institute, The University of Tokyo, Chiba, Japan.